

## L204: A GRAVITATIONALLY CONFINED DARK CLOUD IN A STRONG MAGNETIC ENVIRONMENT

CARL HEILES

Astronomy Department, University of California, Berkeley

Received 1987 April 10; accepted 1987 June 26

## ABSTRACT

L204 is a filamentary dark cloud located in the H I expanding shell associated with the North Polar Spur. We have measured the magnetic field strength in the surrounding H I from Zeeman splitting of the 21 cm line. The average line-of-sight component of magnetic field,  $B_{\parallel}$ , in the H I is  $4.2 \mu\text{G}$ . Using the observed tendency for  $B_{\parallel}$  and the H I velocity to correlate, we argue that variations in  $B_{\parallel}$  result primarily from projection effects, that the total field strength in the H I is  $\sim 12 \mu\text{G}$ , and that magnetic pressure dominates gas pressure. We argue that Alfvén waves might be responsible for the observed tendency for  $B_{\parallel}$  and the H I line width to be anticorrelated. We estimate the field strength in the molecular portion of L204 itself and argue that the small enhancement found within the dense filament is consistent with theoretical expectation. Magnetic braking should have occurred for the component of rotation perpendicular to the magnetic field.

*Subject headings:* interstellar: magnetic fields — nebulae: individual (L204) — radio sources: 21 cm radiation — Zeeman Effect

## I. INTRODUCTION. L204 AND ITS ENVIRONMENT

The Lynds 204 dark cloud (Lynds 1962), shown in Figure 1, is a long, filamentary structure  $\sim 4^{\circ}$  long and  $\sim 15'$  or less wide. The long axis runs along a line of constant right ascension; hereafter we refer to the “top” of the cloud as the northern portion and the “left-hand side” as the eastern portion. At the adopted distance of 170 pc, these angles correspond to  $\sim 12$  and  $0.75$  pc, respectively. Molecular lines allow precise measurements of velocity and rough estimates of mass and volume density; polarization of optical starlight allows maps of the magnetic field direction (McCutcheon *et al.* 1986; hereafter MVDC).

The total mass is  $\sim 400 M_{\odot}$ . The mass per unit length  $\mathcal{M}$  ranges from a maximum of  $\sim 40 M_{\odot} \text{ pc}^{-1}$  downward by about one order of magnitude. The  $\text{H}_2$  volume density  $n_{\text{H}_2}$  ranges downward from a maximum of  $\sim 1400 \text{ cm}^{-3}$ . MVDC found that three important quantities are correlated. One, the radial velocity  $V_{\text{LSR}}$  is correlated with  $\mathcal{M}$ . Two, the filament is not straight. Instead, it has the shape of the letter “S” greatly stretched top-to-bottom. The radial velocities show a strikingly similar behavior, in that the portions of the cloud displaced to the right have more positive radial velocities, and vice versa. Thus, *all three variables*— $\mathcal{M}$ ,  $V_{\text{LSR}}$ , and angular displacement from a straight line—are correlated. The correlation of angular displacement and  $V_{\text{LSR}}$  allowed MVDC to argue that the angular displacement is caused by the projection of the total velocity vector on the sky, and  $V_{\text{LSR}}$  is caused by its projection on the line of sight—i.e., that the velocity vector is oriented neither parallel nor perpendicular to the line of sight. It also allowed them to argue that the structure cannot be a sheet seen edge on, but instead must be filamentary.

The optical polarization vectors trace out the magnetic field, which tends to be roughly horizontal. This makes the field direction in L204 close to the average direction over the  $\sim 1000 \text{ deg}^2$  surrounding territory, as if the density enhancement in the filament has not affected the direction of the magnetic field very much. This horizontal field tends to be roughly

perpendicular to the long axis of the filament, *if* the direction of the long axis is defined by averaging over the whole length of the filament. In shorter sections, however, this perpendicularity is not strictly followed. In the shorter sections that exhibit large lengthwise velocity gradients, the field is oriented at  $\sim 45^{\circ}$  to the local filament, and for one star the field actually lies parallel to the local filament.

L204 lies  $\sim 14^{\circ}$  from the Ophiuchus dark cloud and has almost the same average radial velocity. The Ophiuchus dark cloud has filaments whose length/width ratios are somewhat smaller than that of L204. The Ophiuchus filaments are oriented at  $60^{\circ}$ – $90^{\circ}$  with respect to the L204 filament. The magnetic field directions are roughly the same in the two regions, which makes the magnetic field roughly *parallel* to the Ophiuchus filaments, opposite to the rough *perpendicularity* for the L204 filament. In samples of other filamentary dark clouds, field orientations tend to be either parallel or perpendicular to filament axes (e.g., Vrba, Strom, and Strom 1976).

The H I near L204 is centered near the same velocity as L204 itself,  $\sim 3 \text{ km s}^{-1}$ . We have carefully inspected the H I emission at this velocity over  $\sim 1500 \text{ deg}^2$  centered on L204. There is no local H I excess around L204. The H I photographs of Colomb, Pöppel, and Heiles (1980) show that the H I in the vicinity lies in a shell. This shell is expanding at  $15$ – $30 \text{ km s}^{-1}$  and is associated with the North Polar Spur, which was formed  $\gtrsim 1 \text{ Myr}$  ago (Borken and Iwan 1977; Heiles *et al.* 1980). At L204's typical velocity of  $\sim 3 \text{ km s}^{-1}$ , L204 appears to lie near the edge of the H I shell. At lower velocities, the H I shell is larger in angular size and L204 lies well inside the apparent boundary of the H I shell. At  $V_{\text{LSR}} = 0 \text{ km s}^{-1}$ , the shell radius appears to be  $\sim 80^{\circ}$ , and L204 lies  $\sim 30^{\circ}$  from the edge. If the shell were perfectly spherical and homogeneous, we could go on to calculate the line-of-sight component of the expansion velocity of the L204 region and other related quantities. However, an attempt to do this gives results that are inconsistent with those derived from the large-scale H I structural properties of the shell. This is expected: densities vary widely in

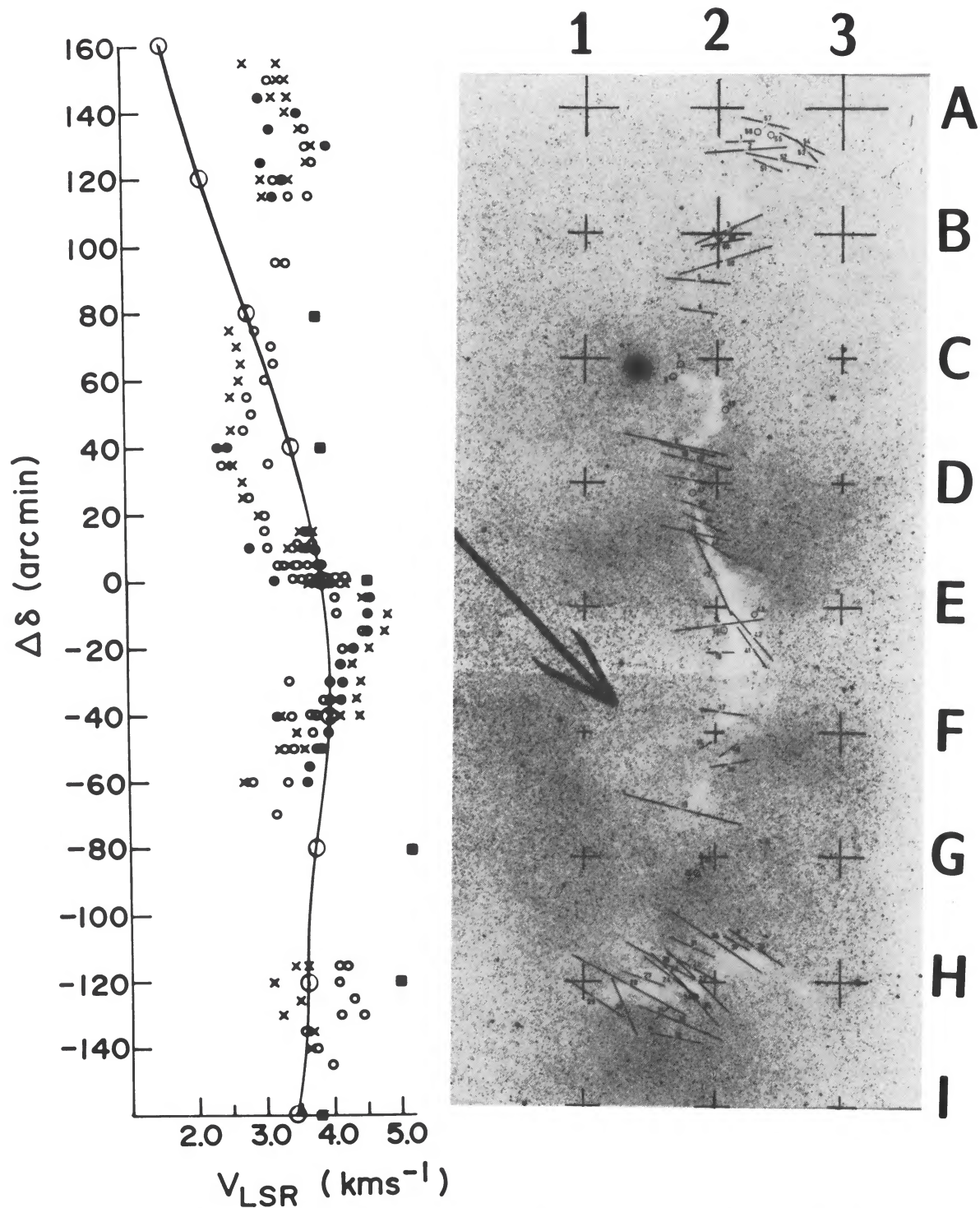


FIG. 1.—Photograph of L204, together with CO velocities (the multitude of individual points) from MVDC. Positions we observed are identified in matrix-like notation by the numbers and letters on the top and right-hand side of the figure: e.g., the bottom-right point is point 3I. The reference position is  $(\alpha, \delta) = (16^{\text{h}}45^{\text{m}}, -12^{\circ}00')$ . The large arrow points toward the center of the North Polar Spur (Berkhuijsen, Haslam, and Salter 1971). H I velocities for the narrow H I emission peak, determined from a double-Gaussian fit (one for the broad low-velocity shoulder, one for the narrow peak) are shown superposed on the CO velocities by the solid line and the small circles. These H I velocities are for the middle of the three positions observed at each declination. H I velocities for the self-absorption components listed in Table 1 are shown by solid squares; these are the average velocities for the three positions. Values of single-fit magnetic fields  $B_{\parallel}$  for all of the 27 observed grid points are indicated by the sizes of the plus signs, which are linearly proportional to the field strengths; for position 3A at the top right,  $B_{\parallel} = 9.1 \mu\text{G}$ , the largest observed value.

the ISM, and, in particular, L204 is a region of enhanced density, so it should have a smaller expansion velocity than most of the shell.

In summary, the overall properties of the H I shell contribute little to the understanding of the L204 region, except to tell us that it is on the far side of the expanding H I shell and that there is no concentration of H I around L204 itself.

The fact that the field direction within L204 is the same as that outside L204 argues that the field is strong enough to dominate the gas dynamics. We also suspect a strong field on the basis of previous Zeeman-splitting studies of the two expanding shells so far studied (neither of which is the North Polar Spur shell), which show that magnetic pressure dominates gas pressure in the swept-up (Troland and Heiles 1982*b*). In this paper we report on measurements of the magnetic field strength in the vicinity of L204 from Zeeman splitting of the 21 cm line of H I. Our results corroborate the strong-field expectation.

## II. OBSERVATIONAL TECHNIQUES

Observations were obtained using the Hat Creek 85 foot telescope and 1024 channel autocorrelator. The telescope HPBW  $\approx 36'$ . The correlator was split into two independent 512 channel banks, simultaneously observing opposite circular polarizations. The sense of polarization was switched at  $\sim 5$  s intervals by a motorized waveguide switch. The total bandwidth was 625 kHz ( $132 \text{ km s}^{-1}$ ); after Hanning smoothing, the velocity resolution was  $0.52 \text{ km s}^{-1}$ . Typical integration times per point were  $\sim 12$  hr. Further details and a description of the data reduction procedure are given in Heiles and Stevens (1986).

For the ubiquitous 21 cm line, circular polarization of the telescope main beam and sidelobes can produce spurious effects (Troland and Heiles 1982*a*). The polarized sidelobes extend over very large solid angles in the sky. They tend to produce broad wiggles in the Stokes  $V$ -parameter spectrum ( $V$  is the difference between the two circular polarizations); these wiggles depend on the time of year. The explicit evaluation of this difference is a large computing job, and we have not performed this task for the present observations. This is justified because the present observations are concerned with a fairly narrow H I line. In addition, observations have been taken at several different times of year and they are perfectly consistent from one observing run to another.

"Beam squint," in which the two circularly polarized beams point in slightly different directions, occurs when the feed is not pointing toward the vertex of the paraboloid. This can happen because of gravitational and thermal deflection of telescope feed legs; we have experimentally measured these deflections and found them to be significant. We have greatly reduced them by installing servo-controlled feed motors. A laser beam from the vertex is pointed at a mirror on the feed, which reflects the beam back to the vertex. The position of the reflected beam is detected by a quadrant detector, which generates an error signal when the beam does not fall on the center of the detector. The error signal is sent to the feed motors, which change the feed angle to eliminate the error signal. The accuracy with which this system works can be measured by observing an unpolarized continuum source. We routinely conduct such test observations periodically throughout each observing run. We typically find that the beam squint—defined as the difference between the directions that the two circularly polarized beams point—is no more than  $1'6$ , or  $\sim 7.5 \times 10^{-4}$  the half-power

beamwidth of the telescope. This is small enough to be of no concern for most measurements, including those reported here.

## III. OBSERVATIONAL RESULTS

We observed a total of 27 positions on a  $3 \times 9$  grid aligned parallel to the cylinder axis, shown in Figure 1. The positions are  $40'$  apart and are designated in matrixlike notation with the numbers and letters shown on Figure 1. Zeeman splitting was detected at every position. Magnetic field strengths were derived by least-squares fitting the entire  $V$  profile to the entire  $I$  profile in the manner described by Heiles and Stevens (1986). In this technique, a *single* magnetic field is assumed to characterize the *entire* H I profile; we denote this the "single-field fit." The magnetic field strengths ranged from  $+1.4$  to  $+9.1 \mu\text{G}$ . The positive signs indicate that the field points away from the observer.

The average for all 27 positions is shown in Figure 2. The net integration time in this average profile is  $\sim 320$  hr. The magnetic field strength derived by the single-field fit is  $+4.1 \pm 0.1 \mu\text{G}$ . The dotted line in Figure 2 shows the  $V$  profile expected from this field strength. It is a good, but not a perfect, match to the observed  $V$  profile. A better match can be obtained by fitting the observed  $I$  profile by three Gaussians and fitting a separate field strength to each Gaussian. Two of these Gaussians fit the narrow, strong portion of the profile, and one fits the broad, weak low-velocity wing. There are two choices for the narrow fit: two Gaussians in emission, or one in emission and one in absorption (corresponding to H I self-absorption).

TABLE 1  
EMISSION (EM) AND ABSORPTION (ABS) GAUSSIAN PARAMETERS  
FOR POSITIONS EXHIBITING OBVIOUS SELF-ABSORPTION

Position	$T$ (K)	FWHM ( $\text{km s}^{-1}$ )	$V_{\text{LSR}}$ ( $\text{km s}^{-1}$ )	$B$ ( $\mu\text{G}$ )
Average: EM .....	52.9	10.4	3.1	4.2
Average: ABS .....	-9.6	3.3	4.3	7.6
1C: EM .....	82.1	8.7	3.5	5.6
1C: ABS .....	-35.1	4.4	3.8	5.7
2C: EM .....	78.2	9.2	3.1	4.1
2C: ABS .....	-31.4	4.4	3.6	5.2
1D: EM .....	70.9	8.6	3.6	3.5
1D: ABS .....	-27.7	3.8	3.8	3.6
2D: EM .....	77.4	10.0	3.6	4.4
2D: ABS .....	-20.0	4.1	3.9	7.5
1E: EM <sup>a</sup> .....	47.4	9.2	3.3	3.0
1E: ABS <sup>a</sup> .....	-4.0	1.8	4.3	-2.3
2E: EM .....	47.2	10.1	3.8	2.4
2E: ABS .....	-5.9	1.6	4.6	11.5
3E: EM .....	49.3	9.8	3.8	3.9
3E: ABS .....	-4.8	2.2	4.3	9.5
2G: EM .....	51.7	9.6	3.9	2.7
2G: ABS .....	-9.5	2.9	5.2	1.4
3H: EM .....	50.6	10.8	3.9	5.0
3H: ABS .....	-6.4	2.7	5.0	13.8
1I: EM .....	83.4	10.1	3.4	5.4
1I: ABS .....	-43.6	6.1	3.7	10.4
2I: EM .....	66.6	10.8	3.5	4.1
2I: ABS .....	-28.3	5.2	3.7	7.0
3I: EM .....	59.2	10.9	3.7	2.5
3I: ABS .....	-17.5	4.1	3.9	3.6

<sup>a</sup> No good least-squares fit could be found for position 1E; the tabulated values do not reproduce the observed  $V$  spectrum well. See Fig. 3*a*.

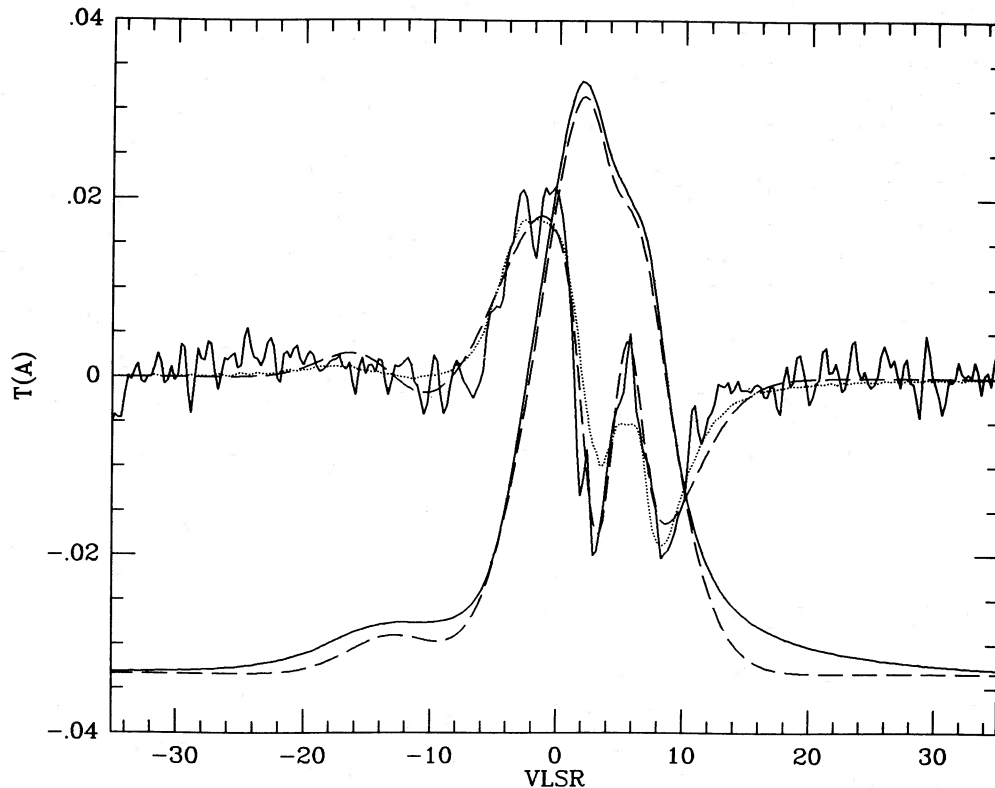


FIG. 2.—Frequency-switched and polarization-switched (Stokes parameter  $V$ ) profiles, averaged over the 27 positions. The smooth solid line is the frequency-switched profile; the dashed line adjacent to it is the fit of three Gaussians, one for the low-velocity shoulder and two for the narrow peak. One of the narrow Gaussians is in self-absorption. The noisy solid line is the  $V$  profile, and the dashed line following it is the fitted with different magnetic field strengths for each Gaussian. All Gaussian parameters are given in Table 1. The dotted line is the single-field fit to the  $V$  profile. Units are antenna temperature,  $T(A)$ , in Kelvins and  $V_{LSR}$  in  $\text{km s}^{-1}$ . The vertical scale applies only to the  $V$  profile; for the  $I$  profiles, the maximum antenna temperature is 49.8 K.

The latter case, with one Gaussian in self-absorption, produces a much closer fit to the observed  $V$  spectrum than the former; this fit is shown by the dashed line in Figure 2, and the Gaussian parameters are given in Table 1.

For the double-Gaussian fit to the narrow H I emission peak, the emission Gaussian has  $B_{\parallel} = 4.2 \pm 0.1 \mu\text{G}$ , very close to the  $4.1 \mu\text{G}$  of the single-field fit.<sup>1</sup> The absorption Gaussian has  $B_{\parallel} = 7.6 \pm 0.3 \mu\text{G}$ , nearly twice as large. This may indicate a field amplification in the self-absorption component, which should be colder and denser than the emission component. Unfortunately, we cannot accurately calculate the H I column density of the absorption component because it depends sensitively on the kinetic temperature and geometrical placement of the cold gas with respect to the warm gas along the line of sight. The observed self-absorption may easily be produced by an H I column of as little as, say,  $5 \times 10^9 \text{ cm}^{-2}$ . For any reasonable volume density (e.g.,  $n_{\text{H I}} = 10 \text{ cm}^{-3}$ ), the associated angular scale ( $\sim 4'$ ) is much smaller than the  $36'$  HPBW of our H I observations. Clearly, more certain statements concerning these self-absorption components require additional observations with much higher angular resolution.

For nearly all individual positions, the single-field fits were very good—roughly of the quality shown in Figure 2 (although of course much more noisy). This was true even if the line

<sup>1</sup> Gaussian parameters for the broad, low-velocity shoulder are:  $T = 3.2 \text{ K}$ ,  $\text{FWHM} = 8.1 \text{ km s}^{-1}$ ,  $V_{LSR} = -13.9 \text{ km s}^{-1}$ ,  $B_{\parallel} = 8.0 \pm 1.5 \mu\text{G}$ . While the derived magnetic field is, formally speaking, significant, we have little confidence in it because instrumental effects may be important at this level.

shapes were not simple Gaussians. However, for some positions there was structure in the  $V$  profile that was not matched by the single-field fit, as if narrow velocity components in the  $I$  profile had detectable magnetic fields. A few examples are shown in Figure 3, which presents results for four individual positions. The particular results shown were selected for the following reasons: position 1E, the only result for which no good  $V$ -profile fit was possible; 1I, the position for which the three-Gaussian fit was best, relative to the single-field fit, as compared to other positions; 3E, illustrative of a typical single-fit result (but noisier than most); 1F, the weakest single-fit field, of marginal statistical significance. Position 1I is anomalous, as compared to most other positions exhibiting obvious self-absorption, in that there seem to be several very narrow self-absorption components spread over a relatively wide velocity range; this exhibits itself as a wider-than-average self-absorption Gaussian in Table 1. We emphasize that most positions had fits of good quality, with better signal-to-noise than for position 3E; we have *not* attempted to present an optimistic “typical” profile, but rather the opposite.

In most of these cases the signal-to-noise ratio was large enough to fit the profile with one or more Gaussian components and fit each Gaussian component with a separate field, as discussed above for the average profile in Figure 2. As for the average profile, we used a total of three Gaussians—one to represent the broad low-velocity shoulder and two to represent the well-defined narrow peak. We found that, as for the average profile, two Gaussians with one in self-absorption reproduced the observed  $V$  profiles significantly better than

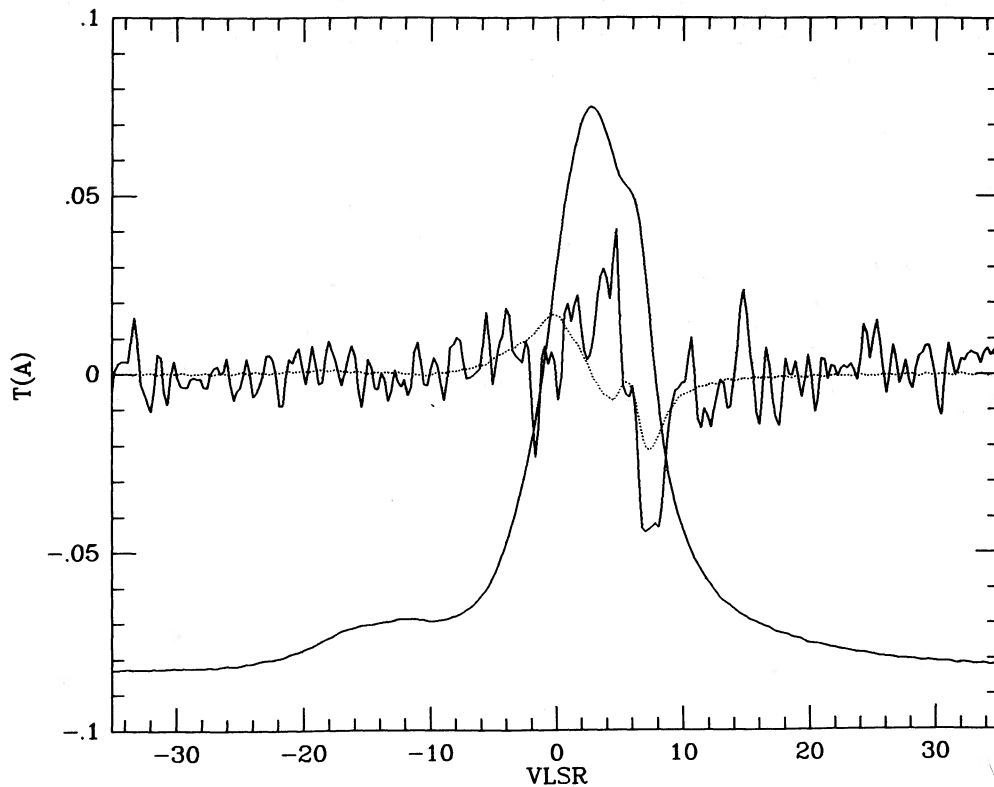


FIG. 3a

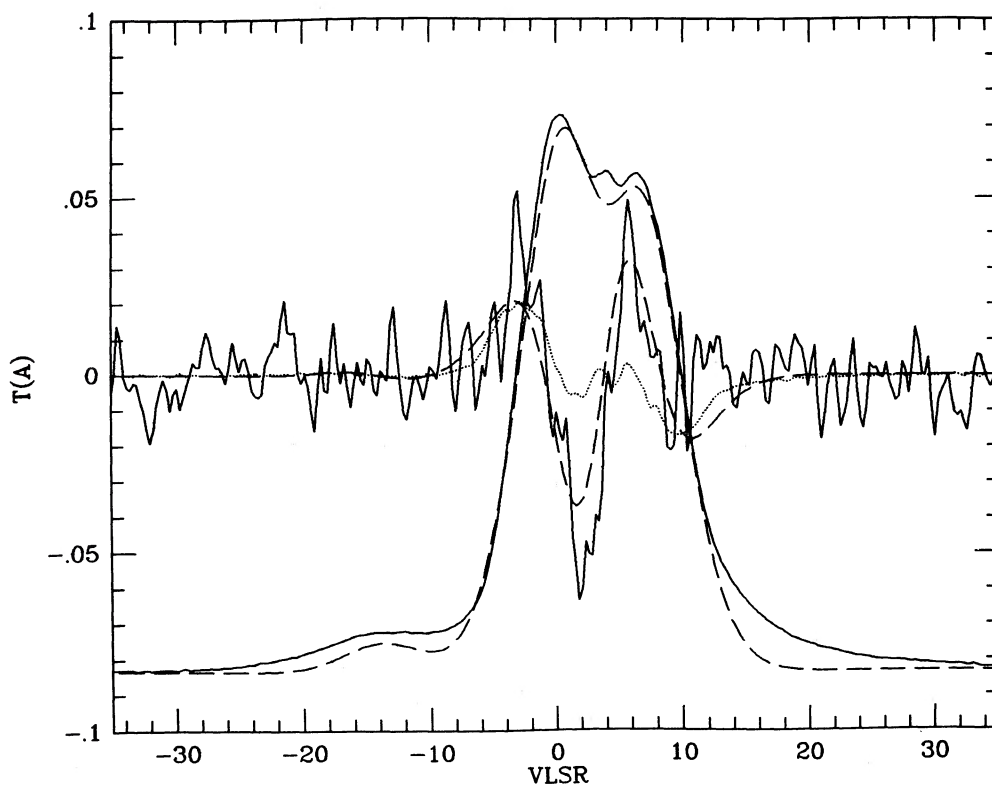


FIG 3b

FIG. 3.— $I$  and  $V$  profiles for four individual positions, selected for the reasons outlined in the text; these profiles are not representative of typical results. Dashed and dotted lines are as in Fig. 2. Note that the vertical scale is 2.5 times larger than for Figure 2. The vertical scales apply only to the  $V$  profiles; for the  $I$  profiles, the maximum antenna temperatures all lie between 46.9 and 48.2 K. Figs. 3a, 3b, 3c, and 3d correspond to positions 1E, 1I, 3E, and 1F, respectively.

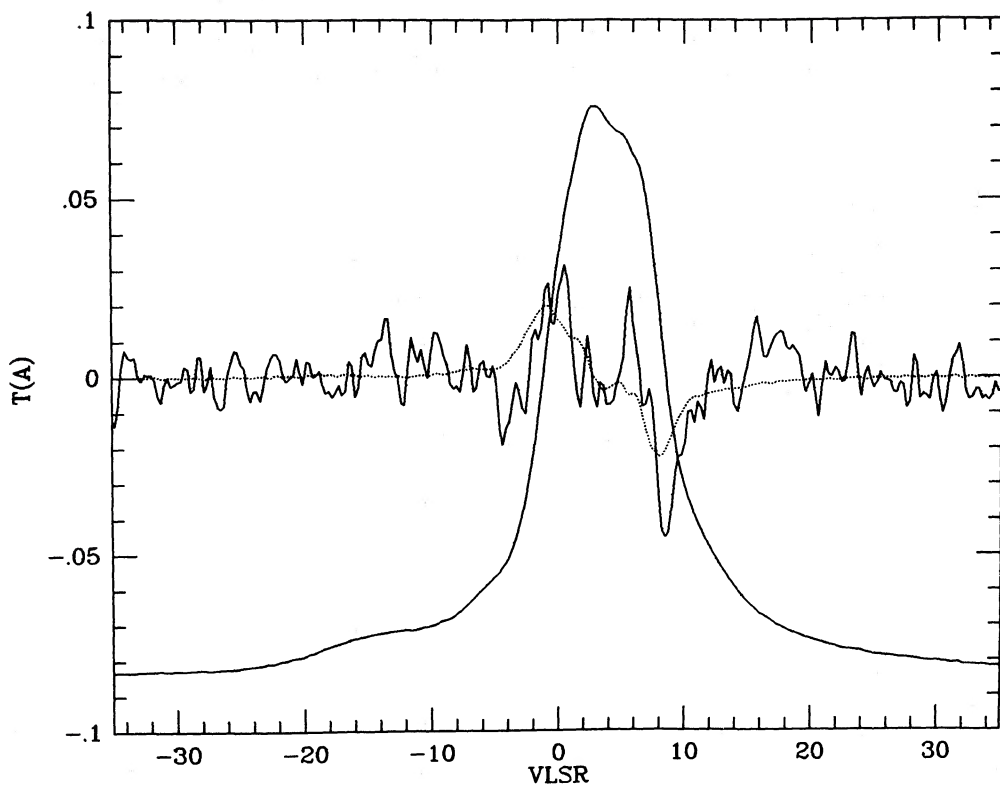


FIG. 3c

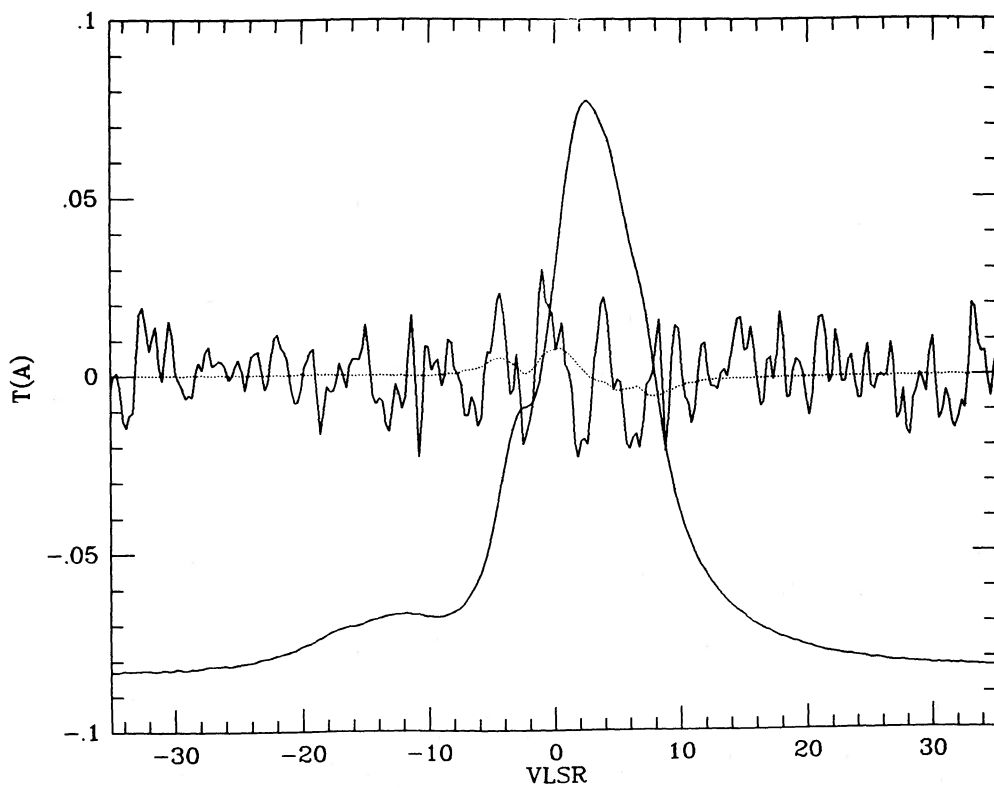


FIG. 3d

two Gaussians with both in emission. The parameters of these Gaussians, together with the derived magnetic fields, are given in Table 1 for those positions that exhibited clear self-absorption.

The least-squares field strength fits for the individual positions behave in a similar way as that for the average profile in Figure 2, discussed above. In all self-absorption cases, the magnetic field associated with the emission component differs insignificantly from that derived from the single-field fit. In about half the cases the field for the self-absorption component also differs insignificantly. However, in the other half, the field for the self-absorption component is about twice the single-fitted field, as if the field is enhanced in some of the regions of cold, dense H I. The existence of this stronger field is not correlated with either the strength or width of the self-absorption component. It is correlated with position: the positions showing stronger self-absorption fields tend to bunch near the middle and middle-right of the region, and near the bottom and bottom-left. See Table 1 for details. As for the average profile, we cannot accurately calculate the column density associated with the self-absorption component.

Figure 1 contains symbols that indicate the single-field fit result for each position. The field is strongest at the top and reaches a minimum near the middle, where both  $\mathcal{M}$  and the lengthwise velocity gradient in L204 are largest, as if one or both of these properties of the molecular filament produces the largest perturbation in the ambient magnetic field. As discussed below, the filament is probably gravitationally bound.

H I velocities were derived by fitting two Gaussians to the I

profiles—one broad Gaussian to represent the broad low-velocity shoulder, and one narrow Gaussian to represent the narrow peak. These H I velocities, together with MVDC's CO velocities, are also shown in Figure 1 and compare fairly well. However, there are significant differences, typically amounting to  $\sim 1 \text{ km s}^{-1}$  or less. L204 is apparently subject to an external H I wind. The velocities derived in this way, which neglect the influence of the self-absorption component, are typically  $\sim 0.07 \text{ km s}^{-1}$  smaller than those obtained for the emission peak when another Gaussian representing the self-absorption is included. This difference is insignificant for all aspects of the discussion.

Velocities of the H I self-absorption components are shown by the filled black squares in Figure 1. These also, exhibit significant differences from the CO velocities. Thus, the self-absorption components do not arise from residual H I located in the molecular portion of L204. The disagreement of H I self-absorption velocities with molecular velocities is a common occurrence in regions such as L204 (Shuter, Dickman, and Klatt 1987).

There is a tendency for the measured magnetic field strength to be correlated with the radial velocity  $V_{\text{LSR}}$ . This is shown in Figure 4. There is scatter in this correlation, but the trend seems unmistakable. A least-squares fit, shown by the dashed line in Figure 4, yields

$$B_{\parallel} = 8.86 - 1.55V_{\text{LSR}}. \quad (1)$$

Here  $B_{\parallel}$  is the measured magnetic field, equal to the component parallel to the line of sight.

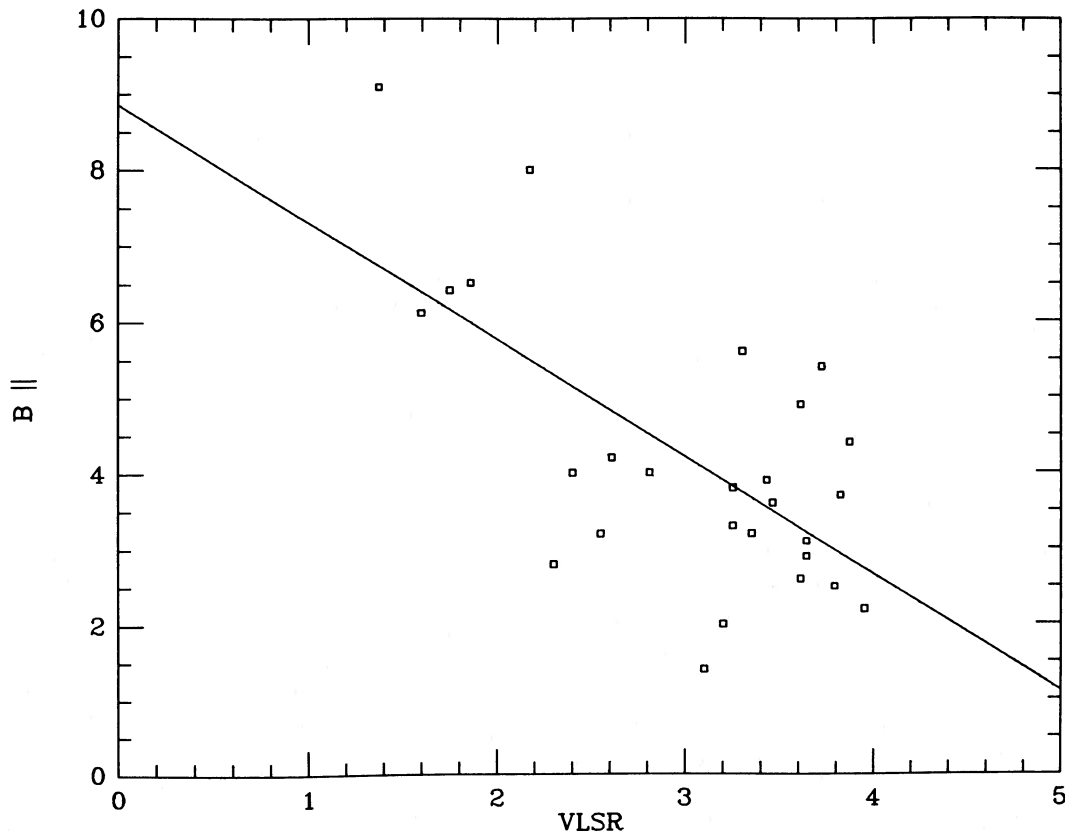


FIG. 4.— $B_{\parallel}$ , derived from the single-field fit, vs.  $V_{\text{LSR}}$  for single Gaussians representing the narrow H I peaks for the 27 observed positions. The line is the least-squares fit (eq. [1]).

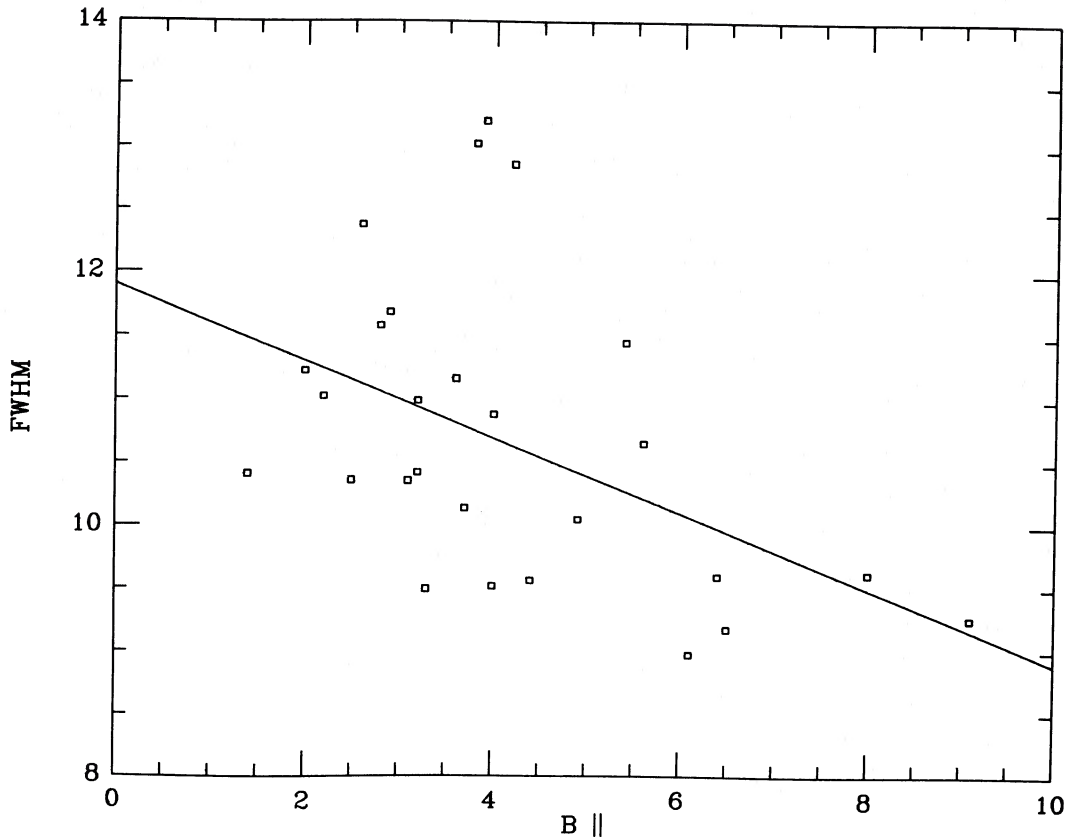


FIG. 5.—Width of single Gaussians representing the H I peaks vs.  $B_{\parallel}$  for the 27 observed positions. The line is the least-squares fit (see text following eq. [1]).

There is also a tendency for the velocity width of the H I profile to be correlated with the magnetic field (and, because of eq. [1], with  $V_{\text{LSR}}$ ). This is shown in Figure 5. A least-squares fit, shown by the dashed line, yields  $\text{FWHM} = 11.9 - 0.30B_{\parallel}$ . There is considerable scatter in this relationship, and the only certain statement is that the five points with largest  $B_{\parallel}$ , i.e., with  $B_{\parallel} > 6 \mu\text{G}$ , have velocity widths FWHM significantly smaller than average. This large scatter should not necessarily be interpreted as a large intrinsic scatter in these variables because both FWHM and  $B_{\parallel}$  are often poorly determined. FWHM can be poorly determined because it results from a least-squares fit of a single Gaussian to a profile that is not always a simple single peak; and  $B_{\parallel}$  can be poorly determined because of statistical noise in the  $V$  profiles.

#### IV. INTERPRETATION

##### a) The Magnetic Environment of L204

Zeeman splitting measurements indicate the line-of-sight component of the magnetic field  $B_{\parallel}$ , not the total field  $B_{\text{tot}}$ . One is always left with the uncertainty whether variations in  $B_{\parallel}$  indicate variations in the strength or the direction of  $B_{\text{tot}}$ . The correlation of  $V_{\text{LSR}}$  and  $B_{\parallel}$  shown in Figure 4 is consistent with variations in direction: both  $V_{\text{LSR}}$  and  $B_{\parallel}$  are projections of total vectors onto the line of sight, and a correlation would result if the gas flows along the field lines.

Thus, we assume that the magnetic field strength is everywhere the same and that variations in  $B_{\parallel}$  result from changes in direction of  $B_{\text{tot}}$ . We cannot determine  $B_{\text{tot}}$ , except insofar as it must be larger than the largest values of  $B_{\parallel}$  measured in the

vicinity. The largest  $B_{\parallel}$  is observed at the upper right-hand corner in Figure 1, and is equal to  $9.1 \mu\text{G}$ . Since the largest value occurs at the corner of the map,  $B_{\parallel}$  is likely to be even higher outside the map boundary. We arbitrarily assume that  $B_{\text{tot}} = 12 \mu\text{G}$  throughout the mapped region.

Theoretically, our picture of constant field strength makes sense if the gas flows along the field lines, which happens if  $B_{\text{tot}}$  is strong enough to dominate the gas dynamics. This is probably the case. At  $12 \mu\text{G}$ , the magnetic pressure  $B_{\text{tot}}^2/8\pi = 5.7 \times 10^{-12} \text{ ergs cm}^{-3}$ ,  $\sim 10$  times the “standard” interstellar gas pressure of  $\sim 5.5 \times 10^{-13} \text{ ergs cm}^{-3}$  (Jenkins, Jura, and Loewenstein 1983). The thermal H I pressure is probably close to the “standard” pressure. Crovisier, Kazès, and Aubry (1980) have measured the H I absorption profile for the radio source PKS 1644–10 (close to our position 2C). From their measurements, we estimate that the H I kinetic temperature  $T_k$  would be  $\sim 80 \text{ K}$  if there were no self-absorption component; the true kinetic temperature must be higher. For  $T_k = 120 \text{ K}$ , the thermal H I pressure would equal the “standard” pressure for  $n_{\text{HI}} \approx 33 \text{ cm}^{-3}$ , which is probably larger than the actual density (see below). Thus, magnetic pressure easily exceeds the thermal gas pressure.

In addition to the thermal pressure, there is the pressure associated with gas turbulence. If this turbulence is isotropic, and if it is wholly responsible for the observed line width of  $\sim 10 \text{ km s}^{-1}$ , then the turbulent pressure amounts to  $\sim 3 \times 10^{-13} n_{\text{HI}} \text{ ergs cm}^{-3}$ . This dominates our estimated magnetic pressure for  $n_{\text{HI}} \geq 17 \text{ cm}^{-3}$ . The H I column density associated with the narrow Gaussian emission peak contains  $\sim 1.1 \times 10^{21} \text{ cm}^{-2}$ .  $n_{\text{HI}} \approx 17 \text{ cm}^{-3}$  corresponds to a distance

along the line of sight of  $\sim 21$  pc, which would amount to  $\sim 7^\circ$  if it were transverse to the line of sight. This seems to be a reasonable scale length of the H I in this direction, so turbulent pressure may be comparable to magnetic pressure.

For  $B_{\text{tot}} = 12 \mu\text{G}$ , the H I gas cannot be in virial equilibrium. For a uniform, spherical cloud with  $B_{\text{tot}}$  decreasing outside the boundary, and under equilibrium between gravity and magnetic forces,  $B_{\text{tot}} \approx 3.4(N_{\text{H I}}/10^{21}) \mu\text{G}$  (Spitzer 1978). For  $N_{\text{H I}} = 1.1 \times 10^{21} \text{ cm}^{-2}$ , our estimated  $B_{\text{tot}}$  is 3–4 times larger than can be contained by gravity. Even though this relation for a spherical cloud does not apply to our aspherical, nonuniform H I structure, the magnetic forces almost certainly dominate gravitational forces. Thus, this region is either confined by external pressure or is (nearly) freely expanding. The former situation is more likely, because of the location of the region in the shock associated with an expanding shell (see § 1).

If our picture that variations in  $B_{\parallel}$  are a result of only geometry and not variations in field strength, then  $B_{\parallel} = 0$  corresponds to the magnetic field being perpendicular to the line of sight. Equation (1) predicts this occurs when  $V_{\text{LSR}} = +5.7 \text{ km s}^{-1}$ . This velocity corresponds to the LSR line-of-sight velocity of the whole magnetically dominated region. Our assumption that  $B_{\text{tot}} = 12 \mu\text{G}$  is equivalent to assuming that H I moves at  $-7.7 \text{ km s}^{-1}$  along the magnetic field—i.e., that the gas moves opposite the direction in which the field points, and if  $B$  were pointing away from us  $V_{\text{LSR}}$  would equal  $-2.0 \text{ km s}^{-1}$ . Smaller  $V_{\text{LSR}}$ 's—motions toward the observer—correspond to motion toward the left on Figure 1. The angle that the magnetic vector makes with respect to the line of sight is just  $\sim \cos^{-1}(B_{\parallel}/12)$ . This angle ranges from  $\sim 40^\circ$  at the top right-hand corner to  $76^\circ$  near the mass concentration in the middle of the map.

Thus, near the top of Figure 1, where the H I velocity is smaller than the CO velocity, the H I is impinging on the CO filament from the right and the rear. Just above the middle, the situation is reversed and the H I impinges on the CO filament from the left and the front. In the dense middle portion the H I impinges on the CO filament from the right and the rear, and in the remainder of the cloud the velocity difference is small. Thus, the H I wind blows in the sense of straightening the filament.

The magnetic field is strong and controls the flow. The magnetic lines connect the CO filament and the diffuse H I. When H I impinges on the CO filament, it cannot flow around the filament because it is tied to the magnetic lines. Thus it must hit the filament and stick to it. The relative flow velocity between the H I and CO is small,  $\sim 1 \text{ km s}^{-1}$ , and is either subsonic or only mildly supersonic. In this case the H I gas should build up a cushion of atomic gas on the outside of the filament. The pressure of this gas should be the ram pressure,  $\approx \rho V^2$ , or  $\sim 2 \times 10^{-14} n_{\text{H I}} \text{ ergs cm}^{-3}$  for  $v = 1 \text{ km s}^{-1}$ . For reasonable values of  $n_{\text{H I}}$ , this is much smaller than the magnetic pressure, which makes the picture reasonable from the theoretical standpoint.

The rate at which the column density of the filament increases is  $\sim 2 \times 10^{-19} n_{\text{H I}} \text{ g cm}^{-2}$  for an impingement velocity of  $1 \text{ km s}^{-1}$ . The rate of column density increase is small for the densest parts of the filament. For example, even for  $n_{\text{H I}}$  as high as  $100 \text{ cm}^{-3}$ , the column density increases by only  $3 \times 10^{20} \text{ cm}^{-2} \text{ Myr}^{-1}$ , an increase of only  $\sim 5\%$  for the densest parts of the filament. The fractional increase for the less dense parts might be much greater. Similarly, the momentum transferred to the filament is small, except perhaps in the less dense portions.

#### b) Self-Gravity and the Magnetic Field in L204 Itself

L204 is almost certainly gravitationally bound. MVDC calculated the gravitational equilibrium of the filament under the approximation that the filament is uniform in density over its entire length. However, this is a poor approximation: MVDC's Figure 5 shows that  $\mathcal{M}$ , the mass per unit length, varies by large factors along the length of the filament.

Accordingly, we tried a different approach. For the lengthwise (top-to-bottom) direction, we treated the filament as five independent clumps and approximated the gravitational field of each clump by that of a point mass. Escape velocities calculated in this way are  $0.54\text{--}0.84 \text{ km s}^{-1}$  for the five clumps, larger than the differences in measured CO radial velocity by factors which average 2.4. If the total velocity vectors lie along the line of sight, the filament could be tilted by  $80^\circ$  to the plane of the sky and still be gravitationally bound; alternatively, if the filament lies in the plane of the sky, the velocities could be as much as  $65^\circ$  from being parallel to the line of sight and the filament still be gravitationally bound.

For the direction across the filament axis, we approximated each clump as a sphere. Typical escape velocities are  $\sim 1.1 \text{ km s}^{-1}$ . Velocity widths are not explicitly given by MVDC. However,  $\text{H}_2\text{CO}$  velocity dispersions  $\Delta$  (defined as  $\exp(-v^2/\Delta^2)$ ) are less than  $0.55 \text{ km s}^{-1}$  (Heiles and Katz 1976) throughout the region. Thus, macroscopic velocities are insufficient to disrupt a clump. The balance is closer for thermal velocities: application of the virial theorem to a uniform  $\text{H}_2$  sphere gives equilibrium for  $T \approx 14 \text{ K}$ , which is probably only slightly larger than the actual kinetic temperature. We conclude, with MVDC, that gravity probably also confines the filament perpendicular to the axis.

MVDC calculated the magnetic field within L204 (i.e., in the molecular portion, not the H I) to be  $\sim 50 \mu\text{G}$ , using the difference between the gravitational and kinetic terms of the virial theorem. In our opinion, their result has poor accuracy. In addition, it is an upper limit, because the gravitational term is an upper limit, having been calculated by assuming that the filament lies in the plane of the sky. If the filament axis is not perpendicular to the line of sight, then the gravitational term is smaller—and so is the magnetic field.

We believe that a better approach is to use the virial theorem for a uniform sphere and assume a balance between gravity and magnetism. This results in the relation  $B \approx 6.8(N_{\text{H}_2}/10^{21})$ , where  $N_{\text{H}_2}$  is the total  $\text{H}_2$  column density within L204. With  $N_{\text{H}_2} \approx 3 \times 10^{21} \text{ cm}^{-2}$ ,  $B \approx 20 \mu\text{G}$ . This is only an approximation, because it depends sensitively on the field geometry, but it does indicate that a value of  $50 \mu\text{G}$  is probably too high.

Suppose that  $B_{\text{tot}}$  near the cloud core, where  $n_{\text{H}_2} \approx 1400 \text{ cm}^{-3}$ , is  $24 \mu\text{G}$ . Then, with  $B \propto n_{\text{H}}^x$ ,  $x \approx 0.15$ . This is much smaller than values of 0.3–0.5 usually quoted. However, in view of the fact that the initial ratio of magnetic to gas pressure before cloud contraction,  $\alpha_i$ , is large—about 10—small values of  $x$  are actually expected from theoretical models (see discussion by Mouschovias 1976).

#### c) Magnetic Braking of L204

L204 seems to be an excellent observational example for the application of models of magnetic braking (see the convenient summary by Mouschovias 1985, and references quoted therein). Its long axis lies perpendicular to the ambient magnetic field. Radial velocities exhibit lengthwise gradients ranging up to  $\sim 2 \text{ km s}^{-1} \text{ pc}^{-1}$  (Fig. 1); this corresponds to rotation with the angular velocity vector *parallel* to  $B_{\text{ambient}}$ ,

where  $B_{\text{ambient}}$  is the field just outside L204. Note that in the most rapidly rotating portion of L204, the local field *within* L204 is *not* perpendicular to the local filament axis. This may well be a disturbance of the field within L204 by the rotation itself, possibly combined with the projection effect of starlight polarization vectors that are highly inclined to the line of sight.

Unfortunately, there exists no published data concerning the velocity gradient *across* the filament, which corresponds to the rotation axis being *perpendicular* to  $B_{\text{ambient}}$ . However, the fact that the CO velocities along the filament axis are reasonably well defined in Figure 1 may imply that rotation in this direction is small.

The time scales for magnetic braking differ greatly for the two directions. For parallel rotation, with velocity gradients along the filament axis, the time scale is  $\tau_{\parallel} \approx 3n_{\text{HI}}^{1/2}$  Myr, where  $n_{\text{HI}}$  is the ambient H I density.  $\tau_{\parallel} \approx 12$  Myr, much longer than the  $\geq 1$  Myr age of the H I shell in which L204 is embedded. For perpendicular rotation, however,  $\tau_{\perp} \approx 0.09n_{\text{HI}}^{1/2}$  Myr, or only  $\sim 0.4$  Myr. Thus, there might well have been time for magnetic braking to be important in the perpendicular direction. This seems to be an ideal test case to search for the oscillatory rotation braking behavior predicted by Mouschovias and Paleologou (1980), which would be revealed observationally by lengthwise variations in the direction of the velocity gradient perpendicular to the filament axis.

#### d) A Bit of Speculation

We now increase our level of speculation and comment about the possible correlation of  $B_{\parallel}$  and FWHM, shown in Figure 5. The sense of this correlation is that FWHM decreases with increasing  $B_{\parallel}$ , i.e., the FWHM is larger when  $B$  is oriented perpendicular to the line of sight. This could be a result of Alfvén waves. Alfvén waves are transverse waves, in which the material moves perpendicular to the field lines. Thus the line-of-sight gas velocity associated with Alfvén waves is largest when the magnetic field is perpendicular to the line of sight. This is just the sense of the correlation shown in Figure 5. Alfvén waves may have been detected near other dark clouds by Shuter *et al.* (1987).

If this interpretation is correct, then the increase in FWHM from 8.3 to 11.9 km s<sup>-1</sup> from  $B$  being parallel to perpendicular

to the line of sight implies transverse wave velocities of 8.5 km s<sup>-1</sup>, or a transverse wave velocity amplitude of  $\dot{x}_A \approx 4.3$  km s<sup>-1</sup>. This is the transverse velocity of the gas, not the Alfvén velocity  $V_A$  itself. If the wave amplitude  $x_A$  is a reasonably small fraction of the Alfvén wavelength  $\lambda_A$ , say  $x_A/\lambda_A < (2\pi)^{-1}$ , then  $\dot{x}_A/V_A < 1$ . With  $\dot{x}_A = 4.3$  km s<sup>-1</sup> and  $B_{\text{tot}} = 12$   $\mu$ G, this corresponds to  $n_{\text{HI}} < 31$  cm<sup>-3</sup>.

The wave amplitude  $x_A$  is then  $\sim 0.7P$  pc, where  $P$  ( $= 2\pi x_A/\dot{x}_A$ ) is the wave period in Myr. If the displacement of the filament from a straight line indicates the Alfvén wave amplitude  $x_A$  in the surrounding H I, then  $P$  would be of order 0.5 Myr since the displacements amount to a fraction of a pc. The Alfvén wavelength would be  $\sim 12n_{\text{HI}}^{-1/2}$  pc; if the wiggles of the filament are sinusoidal, as is weakly suggested by the appearance of the filament on Figure 1, the "wiggle wavelength" of  $\sim 80'$  (4 pc) implies  $n_{\text{HI}} \approx 9$  cm<sup>-3</sup>, which is a reasonable value. These physical parameters are all self-consistent, but we hasten to point out that Alfvén waves, being transverse waves, cannot be responsible for the wiggles in the filament—since the wiggles are displacements *parallel* to the magnetic field.

#### V. WHY DOES THIS FILAMENT EXIST?

As mentioned in the § I, L204 was probably formed in the shock behind the expanding shell associated with the North Polar Spur more than  $\sim 1$  Myr ago. There is no concentration of H I around L204, although L204 is certainly embedded in a large H I structure. There is no apparent reason why a dense molecular filament should have formed at the position occupied by L204, other than the exigencies of random perturbations leading to thermal instability in the compression associated with the shock.

It is a pleasure to acknowledge the assistance of Bon-Chul Koo, who prepared the map of H I surrounding L204 mentioned in § I from the H I survey data of Colomb *et al.* (1980); to W. H. McCutcheon, who provided a high-quality print used in the preparation of Figure 1; and to W. L. H. Shuter for helpfully informative discussions. This work was supported in part by an NSF grant to the author.

#### REFERENCES

- Berkhuijsen, E. M., Haslam, C. G. T., and Salter, C. J. 1971, *Astr. Ap.*, **14**, 252.  
 Borken, R. J., and Iwan, D. C. 1977, *Ap. J.*, **218**, 511.  
 Colomb, F. R., Pöppel, W. G. L., and Heiles, C. 1980, *Astr. Ap. Suppl.*, **40**, 47.  
 Crovisier, J., Kazès, L., and Aubry, D. 1980, *Astr. Ap. Suppl.*, **41**, 229.  
 Heiles, C., Chu, Y., Reynolds, R. J., Yegingil, I., and Troland, T. H. 1980, *Ap. J.*, **242**, 533.  
 Heiles, C., and Katz, G. 1976, *Astr. J.*, **81**, 37.  
 Heiles, C., and Stevens, M. 1986, *Ap. J.*, **301**, 331.  
 Jenkins, E. B., Jura, M., and Loewenstein, M. 1983, *Ap. J.*, **270**, 88.  
 Lynds, B. T. 1962, *Ap. J. Suppl.*, **7**, 1.  
 McCutcheon, W. H., Vrba, F. J., Dickman, R. L., and Clemens, D. P. 1986, *Ap. J.*, **309**, 619 (MVDC).  
 Mouschovias, T. Ch. 1976, *Ap. J.*, **207**, 141.  
 ———. 1985, *Astr. Ap.*, **142**, 41.  
 Mouschovias, T. Ch., and Paleologou, E. V. 1980, *Ap. J.*, **237**, 877.  
 Shuter, W. L. H., Dickman, R. L., and Klatt, C. 1987, in preparation.  
 Spitzer, L. 1978, *Physical Processes in the Interstellar Medium* (New York: Wiley).  
 Troland, T. H., and Heiles, C. 1982a, *Ap. J.*, **252**, 179.  
 ———. 1982b, *Ap. J.*, **260**, L19.  
 Vrba, F. J., Strom, S. E., and Strom, K. M. 1976, *Astr. J.*, **81**, 958.

CARL HEILES: Astronomy Department, University of California, Berkeley, CA 94720